Kinetics of Particle Formation in the Gas Antisolvent Precipitation Process

Nicola Elvassore, Tiziana Parton, and Alberto Bertucco
Dip. di Principi e Impianti di Ingegneria Chimica, Università Padova, 9 I-35131 Padova, Italy

Vito Di Noto
Dip. di Chimica Inorganica Metallorganica ed Analitica, Università di Padova, 1 I-35131 Padova, Italy

An original experimental setup based on UV-vis spectroscopy was developed to study the precipitation kinetics of a biodegradable polymer by gas antisolvent processes (GAS). Poly(L-lactide) acid (PLA) precipitations were carried out in a high-pressure optical cell equipped with sapphire windows, working at 1–80 bar and 301.15–307.15 K. The particle formation and precipitation kinetics were investigated in situ by measuring UV-vis absorbance of polymeric particles at a wavelength of 600 nm. They were measured in a batch system at different pressurization rates (different supersaturation conditions). To rationalize the precipitation kinetics in GAS processes, a population balance model was developed considering particle nucleation, growth, aggregation, and settling. Nucleation and growth were represented by the McCabe model, whereas both independent- and nonindependent-kernel Smoluchowski's coagulation equations were used for aggregation. Settling was approximated by a first-order kinetic. Absorbance measurements were related to the second moment of the simulated particle-size distribution, and the kinetic parameters were estimated based on spectroscopic data. The model gave a correct phenomenological representation of all experimental data and fairly predicted the particle-size distribution of the precipitated PLA microparticles.

Introduction

Interest toward gas and supercritical antisolvent precipitation processes is growing in many fields and is related to the production of micro- and nanoparticulate powders useful for biotechnology, electronics, and pharmaceutical applications (Subramaniam et al., 1997; Reverchon, 1999). In particular, the possibility of manufacturing very small particles of pharmaceuticals, such as proteins and biopolymers, at the nanoscale level, by using mild and inert conditions, represents a great improvement over conventional particle-reduction systems. Traditional techniques involving mechanical comminution, lyophilization, and recrystallization of solutes (such as liquid antisolvent, spray drying, and freeze-drying) can lead to problems due to thermal degradation, excessive use of organic solvent, toxicity, and chemical degradation caused by incomplete solvent removal. Therefore, there is much interest in technologies for producing microparticulate powders at mild conditions, particularly for pharmaceuticals, where controlled particle-size distribution and high product quality are essential prerequisites for a successful industrial development.

Gas and supercritical fluid technologies offer a number of processes that could satisfy these particle-design requirements, such as rapid expansion of supercritical solutions (RESS; Matson et al., 1987), precipitation with compressed antisolvent (PCA; Dixon and Johnston, 1993), aerosol-spray extraction system (ASES; Bleich et al., 1994), and gas antisolvent precipitation (GAS, also referred to as SAS in the case when the antisolvent is at a supercritical state; Gallagher et al., 1988). Among them, PCA, ASES, GAS, and SAS by CO_2 as an antisolvent are widely studied (see, for example, the reviews by Reverchon and Perrut, 2000; Reverchon, 1999). Particularly, these processes have been proposed for the formation of nano- and micro-particles of bio-polymers, proteins, genetic materials, pharmaceuticals, superconductors and catalysts (Reverchon, 1999). Most of these contributions are mainly focused on potential applications of gas antisolvent techniques as effective alternatives to conventional particle-size reduction methods.

Correspondence concerning this article should be addressed to N. Elvassore.

In order to design and to scale the gas antisolvent process up to the industrial stage it is of paramount importance to get a rational understanding of all phenomena involved. Namely, for engineering design of industrial units, it must be understood how the particle characteristics, in terms of morphology and size distribution, are affected by the process variables. However, the theoretical investigation of such processes is rather complicated, as it involves thermodynamics and phase equilibria, mass transfer, jet hydrodynamics (if a semicontinuous process is proposed), and particle-formation kinetics. So far, these basic phenomena were addressed only separately, and mostly thermodynamics (Lora et al. 2000) or mass transport (Werling and Debenedetti, 1999, 2000) are concerned. The kinetics of particle formation, which in general involves three mechanisms (nucleation, growth, aggregation), was rarely addressed despite its enormous importance in characterizing the final product. Recently, Mazzotti et al. (2000) reported an interesting experimental study about nucleation and growth features in batch GAS precipitation experiments. They showed that, depending on supersaturation conditions, that is, CO_2 addition rate, different particle-size distributions (PSD) can be obtained, ranging from narrow unimodal PSD to wide multi-modal ones. These results were qualitatively interpreted by means of a secondary nucleation, and the possibility that aggregation of particles could occur was not considered.

On the other hand, aggregation and breakage mechanisms have been considered in conventional crystallization units only in the last decade. Aggregation is a phenomenon by which two particles collide and adhere to form a new, larger particle. It is indeed a relevant particle-size enlargement mechanism that may significantly affect the PSD of the final product. Its contribution should be taken into account when modeling gas antisolvent precipitation, especially for polymer solutes where microparticles may undergo flocculation and agglomeration, as observed and reported in many studies (Kim and Johnston, 1987). Surprisingly, so far to our knowledge, aggregation has not been taken into account in gas antisolvent processes.

With the aim of investigating both nucleation, growth, and aggregation in the gas antisolvent precipitation process, we propose a simple experimental technique based on UV-vis spectroscopy to follow the time course of the precipitation kinetics in a batch process, and a population balance model to characterize and correlate our experimental measurements.

The need to follow *in situ* the behavior of the precipitation kinetics at high pressure can be satisfied by several experimental alternatives. In recent years, UV-vis spectroscopy has been largely used to monitor supercritical processes *on line*. Simple experimental setups were developed to investigate the polarity of supercritical mixtures (Kim and Johnston, 1987; Kelley and Lemert, 1996), the solubility of dyes (Draper et al., 2000), the pH of water$-CO_2$ solution (Toews et al., 1995), and the volume expansion of saturated liquid phase in GAS process (Elvassore et al., 2001).

In this work, the kinetic of precipitation was followed by measuring *in situ* the attenuation of a light beam passing through a high-pressure optical cell, by means of a UV-vis spectrometer. The attenuation of light due to the scattering of the suspended particles was monitored during the entire precipitation process by measuring the absorbance of a monochromatic beam at a wavelength of 600 nm. This simple technique, which requires only the use of a conventional absorption spectrometer, is commonly applied in turbidimetry to measure the concentration of particulate matter in suspension (Ingle and Crouch, 1988).

The precipitation kinetic data are measured at different pressurization rates, and consequently different supersaturation conditions. A simple correlation between the absorbance of the system, the particle cross section, and the particle-size distribution is proposed.

In order to understand and rationally characterize the precipitation of a model polymer, nucleation, growth, aggregation, and settling phenomena were simultaneously studied through a population balance model. The model is based on the well-known population balance, or particle-number continuity equation, proposed by Randolph and Larson (1988)

$$\frac{\partial n}{\partial t} + \frac{\partial (Gn)}{\partial L} + n\frac{d(\log V)}{dt} = B - D \qquad (1)$$

where n is the population density function, L is the characteristic length of the particles, t is time, and V is the total volume of the system. Equation 1 relates the accumulation of particles of the given size ($\partial n/\partial t$), the convective flux (growth) along the size axis ($\partial Gn/\partial L$), and the generation and the death particle rates, B and D, respectively. The generation term takes into account nucleation and aggregation phenomena, whereas the death one represents both the settling rate and the removal of particles due to aggregation.

In the unseeded precipitation process, Eq. 1 describes the formation of primary nuclei (10–100 nm) that can growth or agglomerate to form aggregates (0.1–10 μm). A parametric study of the model provides useful information about the influence of these single phenomena on the absorbance of the system and on PSD. It will be shown that the experimental measurements can be correlated only if the agglomeration contribution is taken into account.

Experimental Section

Reagents and solution

Spectroscopy-grade organic solvents dichloromethane (DCM) (Aldrich, Steinheim, Germany) were used without further purification. CO_2 99.95% grade purity CO_2 was purchased from Air Liquide (Padova, Italy). Poly(L-lactide) acid (PLA) with molecular weight of 102.000 Da was supplied by Boeringer Ingenheilme (Ingenheilme, Germany). The polymer concentration in the organic solvent solution were of 1.0 % w/w, as normally used in gas antisolvent processes when fine particles have to be produced.

Apparatus and instrumentation

The measurement of the system absorbance was carried out through a UV-vis spectrometer linked to a high-pressure batch apparatus. In Figure 1 the experimental setup is shown. The equipment includes a cooled CO_2 supply system, a high-pressure optical cell, a Perkin-Elmer (Lambda 15) UV-vis spectrometer, and a depressurizing section. The CO_2 supply was ensured by a reciprocating pump (model 305, Gilson,

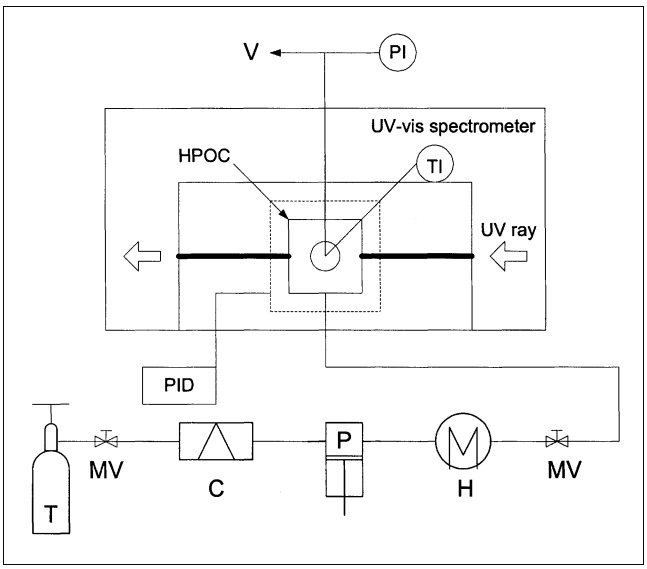

Figure 1. Apparatus used to perform the experimental measurements.

T, CO_2 tank; P, piston pump; C, cooler; H, heater; MV, metering valve; HPOC, high-pressure optical cell; V, vent.

Milano, Italia) and was controlled by fine metering valves (model 1316G4y, Hoke, Creskill, NJ, USA).

Solution samples were loaded into an 8-mL customized stainless-steel cell (SITEC, Zurich, Switzerland) equipped with 4-mm-thick sapphire windows. The upper cap was connected to a pressure-measurement device, a temperature probe, and the outlet line. Upon the addition of CO_2, the volume of the liquid phase may increase by over 1,000% with respect to the initial one. For this reason, the upper cap was provided with an expansion chamber in order to prevent the cell from being filled by liquid. A metallic frit of diameter 3.5 mm with 5-nm porosity (Aldrich, Steinheim, Germany) was placed at the bottom of the cell to obtain a fine CO_2 dispersion through the liquid phase during the pressurization step. The cell temperature was controlled by an electric resistance whose power was regulated using a variable voltage controller.

Internal cell temperature was measured by a Pt 100-Ω resistance. The pressure was continuously monitored through a pressure transducer (model MA 01720, Data Instrument, Acton, MA, USA) with digital readout. Instrument calibration was performed in the range of 293.15–333.15 K and 1–200 bar, and the optical cell temperature was usually maintained at ± 0.1 K with respect to its setpoint value.

Experimental procedure

The cell was sealed and heated up to the desired temperature, and then repeatedly flushed with CO_2 to remove any residual air. Before starting the experiment, a background spectrum of pure CO_2 at 1 bar was recorded for automatic baseline corrections of all subsequent spectra. Three mL of 1% w/w polymer solution were rapidly loaded into the high-pressure cell. The cell was then pressurized by feeding CO_2 from the bottom. Addition of the CO_2 caused the pressure to increase at various rates, ranging from 0.13 bar/min to 0.8 bar/min. During pressurization, the absorbance values at 600 nm were continuously collected. At this wavelength, scattering phenomena can be accurately detected. When the value of absorbance showed a rapid increase due to the initial particle formation within the high-pressure cell, the CO_2 addition was stopped. The evolution of the system was followed by collecting the absorbance profile for the next 90 min. We note that when the onset of polymer precipitation pressure was reached, all valves were immediately closed to separate the optical cell from the rest of the apparatus. In this way, the absence of turbulence and shear stresses could be ensured during precipitation, thus reducing to a negligible level the breakage of formed particles.

This experimental procedure, together with the slow pressurization rates, makes it reasonable to assume quasi-equilibrium conditions for the system at any time. We note also that the expansion of the liquid phase and the pressure of the system do not substantially change after precipitation is started: it was checked that the change in the liquid volume between the onset of precipitation and the end of the experiment was always below 2%, even at the highest pressurization rate investigated. The time course of the liquid-phase volumetric expansion was measured *in situ* by a method recently proposed (Elvassore et al., 2001).

Model Section

Assuming no seed particles at the initial conditions, crystal growth rate independent of crystal size, and constant volume during precipitation, the mathematical description of the precipitation process follows directly from Eq. 1

$$\frac{\partial n}{\partial t} = \left(-G \frac{\partial n}{\partial L} \right)_{\text{growth}} + B_{\text{nucl}} + B_{\text{aggr}} - D_{\text{aggr}} - D_{\text{sett}} \quad (2)$$

where the subscripts refer to growth, nucleation, aggregation and settling, respectively.

Growth

The population balance equation is written according to McCabe ΔL law. This equation states that the growth rate, G, is not a function of length, L, and is, thus, for growth only

$$\left(\frac{\partial n}{\partial t} \right)_{\text{growth}} = -G \frac{\partial n}{\partial L} \quad (3)$$

where n is the population density function.

Nucleation

The nucleation rate, B_{nucl} is assumed to be the rate of appearance of zero-size particles, from which it follows

$$B_{\text{nucl}} = B_0 \delta(L) \quad (4)$$

where $\delta(L)$ is the Dirac delta function and B_0 is the nucleation rate of zero-size nuclei.

Aggregation

The population balance model for aggregation is proposed using the volume, v, as the internal coordinate. The Smolu-

chowski's coagulation equation expressed in continuous space was used for describing the generation and the destruction of particles by aggregation

$$B'(\nu)_{\text{aggr}} = \frac{1}{2}\int_0^{\nu} \beta'(\nu-\epsilon,\ \epsilon)n'(\nu-\epsilon,t)n'(\epsilon,t)\ d\epsilon \quad (5)$$

$$D'(\nu)_{\text{aggr}} = n'(\nu,t)\int_0^{\nu} \beta'(\nu,\ \epsilon)n'(\epsilon,t)\ d\epsilon \quad (6)$$

The prime symbol ($'$) is used as a reminder that volume is the internal coordinate. The coalescence kernel $\beta'(\nu,\ \epsilon)$ is the measure of the collision frequency between particles of volume, ν and ϵ, that are effective in producing a particle of volume $\nu+\epsilon$.

In order to describe simultaneously growth and aggregation, Eqs. 5 and 6 have to be converted in terms of length-based equations (Hounslow et al., 1988; Hounslow, 1990), as follows

$$B_{\text{aggr}} = \frac{L^2}{2}\int_0^L \frac{\beta\left[(L^3-\lambda^3)^{1/3},\ \lambda\right]\cdot n\left[(L^3-\lambda^3)^{1/3},\ t\right]\cdot n(\lambda,t)\ d\lambda}{(L^3-\lambda^3)^{2/3}} \quad (7)$$

$$D_{\text{aggr}} = n(L,t)\int_0^{\infty} \beta(L,\ \lambda)\cdot n(\lambda,t)d\lambda \quad (8)$$

Here $\beta(L,\ \lambda)$ is the coalescence kernel, which is a function of particle size L and λ.

Settling

Particle settling is generally affected by particle size, liquid viscosity, solid and solution density, and for small flocculent particles, by solid concentration. In this work the settling rate contribution was approximated through first-order kinetics (Perry and Green, 1997)

$$D_{\text{sett}} = k_{\text{sett}}L^2 n(L,t) \quad (9)$$

where k_{sett} is the settling constant that accounts for both particle and system characteristics.

The final form of the population-balance equation is given by substituting Eqs. 3–4 and 7–9 into Eq. 2

$$\frac{\partial n(L,t)}{\partial t} = -G\frac{\partial n(L,t)}{\partial L} + B_0 + \frac{L^2}{2}\int_0^L \frac{\beta\left[(L^3-\lambda^3)^{1/3},\ \lambda\right]\cdot n\left[(L^3-\lambda^3)^{1/3},\ t\right]\cdot n(\lambda,t)\ d\lambda}{(L^3-L^3)^{2/3}} - n(L,t)\int_0^{\infty}\beta(L,\ \lambda)\cdot n(\lambda,t)\ d\lambda - k_{\text{sett}}L^2 n(L,t) \quad (10)$$

Numerical solution

Equation 10 cannot be solved analytically. In this work, an adjustable geometric discretization for the population balance equations (Litster et al., 1995) was used for all terms (nucleation, growth, aggregation, and settling). Accordingly, the following system of equations was written

$$\frac{dN_i}{dt} = \left(\frac{dN_i}{dt}\right)_{\text{nucl}} + \left(\frac{dN_i}{dt}\right)_{\text{growth}} + \left(\frac{dN_i}{dt}\right)_{\text{aggr}} + \left(\frac{dN_i}{dt}\right)_{\text{sett}} \quad (11)$$

In Eq. 11, N_i is the number of particles in the ith-length interval. The geometric length-domain discretization has the form of $\nu_{i+1}/\nu_i = 2^{1/q}$, where q is an integer greater than or equal to one.

This discretization allows mesh points to finely cluster in the region where the PSD changes rapidly and, at the same time, to cover a wide length of domain ranging from nanometric initial-nuclei dimension to hundreds of microns.

Accordingly, nucleation and growth rates were modeled using the following equation (Hounslow, 1990; Litster et al., 1995)

$$\left(\frac{dN_i}{dt}\right)_{\text{nucl}} = \begin{cases} B_0, & i=1 \\ 0, & i\neq 1 \end{cases} \quad (12)$$

$$\left(\frac{dN_i}{dt}\right)_{\text{growth}} = \frac{G}{(r-1)L_i}(rN_{i-1}-N_i) \quad (13)$$

where r is the ratio of the upper to lower size limits for each size, $r = L_{i+1}/L_i$, and is equal to $r = (\sqrt[3]{2})^{1/q}$. Other variables have their usual meaning.

Both nucleation and growth rates are functions of supersaturation, S, which can be represented by power laws

$$B_0 = k_n S^a \quad (14)$$

$$G = k_g S^b \quad (15)$$

Supersaturation is defined as $S = (c-c_{\text{eq}})/c_{\text{eq}}$, where c is the concentration of solute in solution; c_{eq} is the equilibrium solubility, k_n, a and k_g, b nucleation and growth kinetic constants, respectively. The agglomeration term that preserves the third moment of the PSD can be expressed according to the model proposed by the Hounslow's group (Litster et al., 1995) and improved by Wynn (Wynn, 1996)

$$\left(\frac{dN_i}{dt}\right)_{\text{aggr}} = \sum_{j=1}^{i-S_1}\beta_{i-1,j}N_{i-1}N_j\frac{2^{(j-i+1)/q}}{2^{1/q}-1} + \sum_{p=2}^{q}\sum_{j=i-S_{p-1}}^{i-S_p}\beta_{i-p,j}N_{i-p}N_j\frac{2^{(j-i+1)/q}-1+2^{-(p-1)/q}}{2^{1/q}-1} + \frac{1}{2}\beta_{i-q,i-q}N_{i-q}^2 + \sum_{p=1}^{q-1}\sum_{j=i+1-S_p}^{i+1-S_{p+1}}\beta_{i-p,j}N_{i-p}N_j\frac{-2^{(j-i)/q}+2^{1/q}-2^{-p/q}}{2^{1/q}-1} - \sum_{j=1}^{i+1-S_1}\beta_{i,j}N_iN_j\frac{2^{(j-i)/q}}{2^{1/q}-1} - \sum_{j=i+2-S_1}^{\infty}\beta_{i,j}N_iN_j \quad (16)$$

where S_p is an integer given by

$$S_p = \text{int}\left[1 - \frac{q \ln(1-2^{-p/q})}{\ln 2}\right] \tag{17}$$

Various expressions can be found in the literature for both size-independent or size-dependent coalescence kernels $\beta_{i,j}$. Many of them have a sound theoretical basis, depending on the system characteristics [that is, Brownian coagulation, coagulation in shear flow, or by gravitational settling (Ernst, 1986)], whereas others are purely empirical. We refer to the following general expression of the coagulation kernel

$$\beta = k_{\text{aggr}}(i+j)^{\omega} \tag{18}$$

where k_{aggr} and ω are aggregation constants.

The kinetics of the settling term of Eq. 9 can be discretized as follows

$$\left(\frac{dN_i}{dt}\right)_{\text{sett}} = k_{\text{sett}} L_i^2 N_i \tag{19}$$

The set of nonlinear ordinary differential equations (ODEs) obtained by discretization was solved using a Fortran 90 code linked to IMSL subroutine DIVPAG, which is particularly suitable for stiff systems of first-order ODEs. This routine uses a variable-order and variable-step method with backward differentiation formulas (BDF). The ODEs are integrated over the same time range of experimental measurements. We note that the population balances are simultaneously solved for nucleation, growth, aggregation, and settling. Two mass balances are considered: one for the particles suspended in the solution and one for the settled particles. At each integration time, the moments of the population density function, N_i, for both suspended and settled particles were calculated and the total mass balance was checked.

For parametric studies a mesh of 200 points with $q = 6$ was used, whereas data regression was carried out with 90 points and $q = 3$ to shorten the computation time. In all cases, the discretized size ranges from 0.1 μm to 200 μm were considered.

The numerical accuracy of the discretized algorithm was tested separately for the different terms of Eq. 2, with reference to the corresponding analytical solutions.

Relation between moments and absorbance

The jth moments of the population density function, defined as

$$m_j = \int_0^{\infty} L^j n(L)\, dL \tag{20}$$

are of particular interest. The first four moments are related, respectively, to the particle averaged-total number N_T; length L_T; area A_T; and volume V_T, per unit of volume of suspension, as follows

$$N_T = m_0 \tag{21}$$

$$L_T = k_L m_1 \tag{22}$$

$$A_T = k_A m_2 \tag{23}$$

$$V_T = k_V m_3 \tag{24}$$

The values of shape factors k_L, k_A, k_V in Eqs. 22–24 depend on particle geometry: under the assumption of spherical particles, $k_L = 1$, $k_A = \pi$, and $k_V = \pi/6$. The concentration of the suspended particles (w/w) c_p, is calculated by

$$c_p = (3\rho_p k_V h) m_3 \tag{25}$$

where ρ_p is the particle density (g/L) and h is a mass correction constant (7.55 10^{-4}L/g).

If we consider a monochromatic incident ray of radiant intensity I_0 passing through a solution containing suspended particles, the attenuation of light due to particle scattering is given by (Ingle and Crouch, 1988)

$$I/I_0 = \exp(-\tau l) \tag{26}$$

where I is the transmitted ray intensity, τ the slurry turbidity, and l the high-pressure cell width (optical path). Equation 26 closely resembles the Lambert–Beer law, as turbidity is usually proportional to the concentration of suspended particles. Hence, as discussed by Rawlings et al. (1993), turbidity can be expressed as a function of the population balance

$$\tau = \int_0^{\infty} n(L) A_P(L) Q(L)\, dL \tag{27}$$

where $A_p(L)$ is the projected area for a particle of characteristic size L, and $Q(L)$ is the extinction efficiency factor. It is assumed that, in gas antisolvent precipitation, the projected area of the particle is primarily responsible for the light scattering effect. In addition, under this approximation, scattering may be considered independent of the refractive index of the solution (Rawling et al., 1993). Hence, Eq. 27 can be related to the second moment of the PSD as follows

$$\tau = \tilde{Q} k_A m_2 \tag{28}$$

where $\tilde{Q}$ is the overall extinction efficiency that takes into account the scattering phenomena of the micrometric particles for all L's (Rawlings et al., 1993). In summary, the absorbance of the system A is given by

$$A = \tilde{Q} k_{\text{exp}} k_A l \int_0^{\infty} L^2 n(L)\, dL \tag{29}$$

where k_{exp} is a constant accounting for the system characteristics. The value of k_{exp} was determined by calibration, using a sample of PLA particles with known PSD in water solution. Note that Eq. 29 neglects the contribution of multiple scattering. Actually, the linear behavior of absorbance was observed at all the different particle concentrations.

All the values of the parameters used for modeling our systems are summarized in Table 1.

Table 1. Experimental and Population Balance Model Constants.

Constant	Description	Value
K_A	Area factor	π
K_V	Volume factor	$\pi/6$
h	Mass correction constant	7.55×10^{-4} L/g
$\tilde{Q}$	Overall extinction efficiency	3
k_{exp}	Absorbance experimental correction	0.002
L_0	Initial nuclei dimension	0.1 μm
l	UV-vis cell optical path	4×10^{-3} m

Results and Discussion

Simulation

Before presenting the results of the precipitation experiments, the model just developed has been used to perform a parametric investigation of the particle-formation kinetics in a gas antisolvent process.

In the batch process investigated, the antisolvent (CO_2) is added to the system at a constant flow rate, and nucleation may not take place until the solute concentration exceeds its saturation value. However, the onset of precipitation occurs only when a value higher than this one (that is, the critical supersaturation limit) is attained. As already mentioned, the CO_2 addition to the system was stopped as soon as the first evidence of precipitation was detected, allowing the system to approach equilibrium conditions in a constant liquid-phase volume hypothesis. During precipitation four phenomena compete: the generation of new nuclei of the solid phase (nucleation), the enlargement of nuclei due to the deposition of solid material on the surface of existing ones (growth), the aggregation of nuclei (or particles), and the settling of formed particles.

Nucleation and growth, being functions of supersaturation, consume the polymer dissolved in the solution. Both of these phenomena increase the average-particle cross section and consequently the absorbance of the system. When nucleation is dominant, the absorbance profile rises sharply, due to the formation of small nuclei at high concentration values. On the other hand, when growth is dominant, the enlargement of the particles (generally slower than the nucleation rate) causes a parabolic increase of the absorbance profile until an asymptotic condition is reached.

Independently of saturation conditions but dependently of particle concentration, first aggregation, and settling later, decrease the absorbance of the system. According to the model currently proposed, the aggregation mechanism preserves the total volume of the solid phase, but reduces the average cross section of the particles (second moment of the PSD). On the other hand, the settling mechanism decreases the absorbance of the system, but becomes significant only for larger particles and only can be dominant at the end of the process.

Since all these phenomena take place simultaneously, the absorbance profile is expected to increase initially, due to nucleation and growth driven by the initial supersaturation, and to decrease afterwards, due to the aggregation and sedimentation depending on particle concentration and size.

To show the competition of nucleation, growth, aggregation, and settling, simulations are presented that refer to cases close to the typical experimental absorbance profile, which was used as a reference. Parameter values are: $k_n = 2.0*10^8$ and $a = 2.0$ for nucleation; $k_g = 1.0\cdot10^{-5}$ and $\omega = 1.6$ for growth; $k_{aggr} = 2.5*10^{-15}$ and $\omega = 1.0$ for aggregation; $k_{sett} = 1.0*10^{-5}$ for settling; and $S = 8.2$ for supersaturation. In this parametric study the parameter values were increased and decreased by 50% with respect to the base case ones.

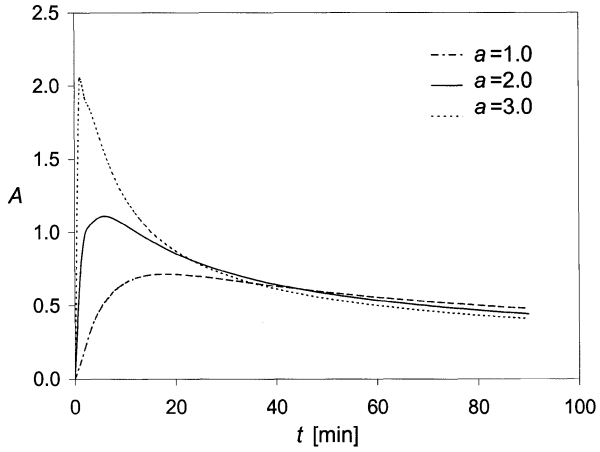

Figure 2. Simulated absorbance profiles as a function of time (solution of Eq. 10); influence of the exponent of the nucleation rate expression *a*.

In Figure 2 the influence of nucleation parameter a is examined. High nucleation rates lead to an elevated initial value of absorbance, corresponding to a high concentration of very small particles. In this case the polymer dissolved in the solution is quickly consumed and the aggregation of small particles is favored, giving (a) sharply decreasing absorbance profile. On the other hand, the particle concentration, and consequently the absorbance, is lower at low nucleation rates. In this case growth becomes the dominant mechanism for particle enlargement. The absorbance rises until the system is supersaturated, then it decreases slowly, as the aggregation rate is low due to the low particle concentration. An analogous absorbance profile is obtained when the other nucleation parameter (k_n) is varied, but the effect is less than for the a parameter.

Figures 3 shows the influence of growth parameter b. The competition between growth and all other mechanisms produces two types of absorbance profile. The first one is similar to that reported for a high nucleation rate, because an increase in the particle cross section is obtained in both cases. The second one has an interesting behavior, because the absorbance profile initially displays two local maxima. This happens at a low growth rate, where the competition between aggregation and growth occurs at longer times. The aggregation contribution becomes dominant and the absorbance of the system decreases monotonically only when the polymer concentration returns to saturation. Note that in all cases the absorbance values are smaller than those shown in Figure 2.

The influence of the aggregation term is considered in Figure 4 by varying the parameter ω. Aggregation parameters largely affect absorbance profiles; in particular, ω mostly changes the profile shape, whereas k_{aggr} acts on the absorbance value at maximum (calculations not reported). In

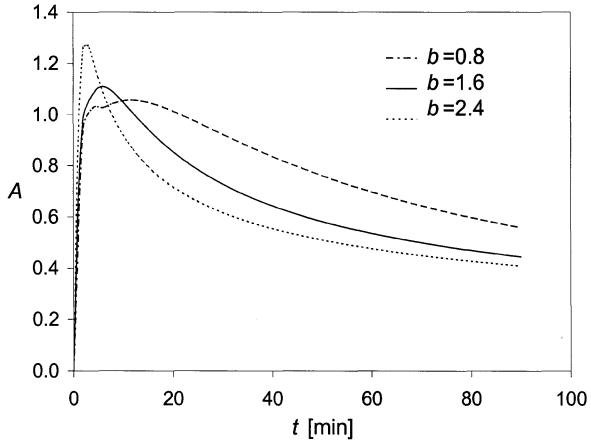

Figure 3. Simulated absorbance profiles as a function of time (solution of Eq.10); influence of the exponent of the growth rate expression *b*.

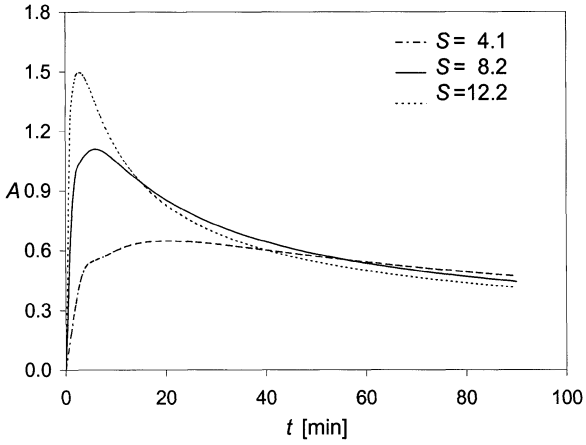

Figure 5. Simulated absorbance profiles as a function of time (solution of Eq. 10); influence of supersaturation, *S*.

the absence of aggregation ($\beta = 0$), the profile reaches an asymptotic value when supersaturation approaches zero. We note that the absorbance profile obtained from the experimental measurements can be reproduced only if the aggregation kernel constant is not zero. This result confirms the occurrence of the aggregation mechanism in our gas antisolvent precipitation process.

The contribution of settling heavily depends on particle dimensions; it can be easily seen that, according to our model, it becomes important at times where bigger particles have been generated by aggregation.

It is interesting to observe that the influence of the supersaturation conditions on the absorbance profile of the system, reported in Figure 5, is related to the ratio between nucleation and the growth parameters of Eqs. 14 and 15, which is generally greater than one. In this case, higher values of supersaturation favor nucleation, whereas lower ones allow particle growth, leading to a parabolic absorbance profile.

In summary, three regimes can be evidenced, depending on the contribution of different kinetic mechanisms. In the first one absorbance increases due to the dominant nucleation phenomena; in the second one it can rise or decrease as a result of the competition between growth and aggregation; and in the third one gravitational settling leads to smooth and constantly decreasing profiles.

It is well known that aggregation can lead to bimodal particle-size distribution. In this respect, two examples of simulated particle-size distribution are reported in Figures 6 and 7, for the cases of dominant aggregation and growth effects, respectively. It is interesting to note that a bimodal distribution is generated for the high value of the aggregation kernel (Figure 6). On the other hand, unimodal distribution with a larger mean particle dimension can be obtained when the growth contribution is dominant, as can be seen in Figure 7. These results can explain the bimodal particle-size distributions experimentally observed in particulate products obtained by batch gas antisolvent precipitation experiments (Mazzotti et al., 2000). Alternately, the bimodal distribution can be justified by accounting for a secondary nucleation mechanism.

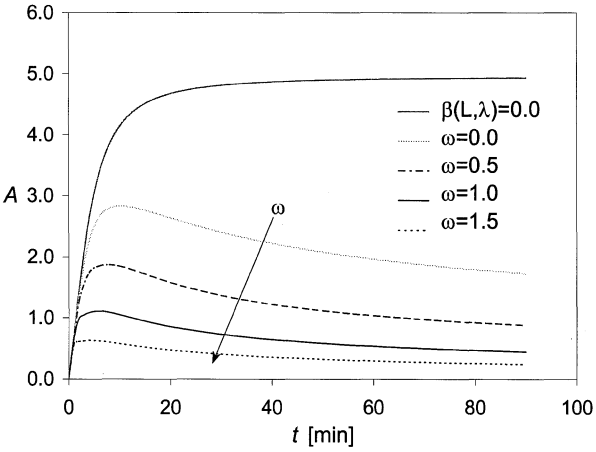

Figure 4. Simulated absorbance profiles as a function of time (solution of Eq. 10); influence of the exponent of the coalescence kernel expression, ω; $\beta(i,j) = 0$ corresponds to the absence of aggregation.

Experiments

In order to investigate the precipitation kinetics of PLA, experimental runs were carried out at 301.15 and 307.15 K, and the absorbance of the system was monitored on-line. In order to provide a set of curves suitable for the evaluation of model parameters, the runs were performed at different pressurization rates, which can be related to supersaturation conditions. In Figures 8 and 9 experimental results are summarized at 301.15 and 307.15 K, respectively; symbols represent the measurements, whereas lines are the model-simulated absorbance profiles at three different pressurization rates.

It is clear that the experimental setup currently proposed allows us to follow accurately the time course of precipitation

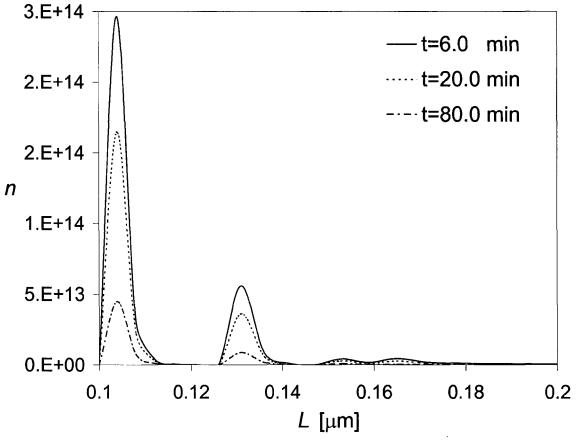

Figure 6. Particle-size distribution as a function of particle size *L* for a case where nucleation and aggregation are the dominant phenomena.

Numerical solution of Eq.10 at three different values of time.

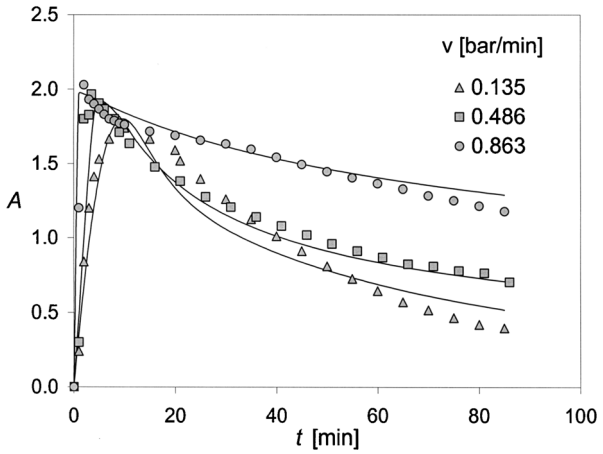

Figure 8. Experimental and calculated absorbance profiles as a function of time for different CO_2 pressurization rates at 301.15 K.

Data points are measured by UV-vis spectrometer for the PLA precipitation from dichloromethane solution. The curves represent the absorbance profile simulated by numerical solution of Eq. 10. The values of model parameters are fitted on the experimental data (see Table 2).

kinetics under pressure. It can be seen that, as already discussed in the model result section, experimental absorbance profiles show different behaviors according to supersaturation level, as shown in Figures 8 and 9. In particular, for high CO_2 pressurization rates, that is, high supersaturation, they rise sharply up to high values: this means a high concentration of small particles, a condition favoring aggregation. Even if the temperature difference is small, a higher temperature leads to higher absorbance values. This behavior is probably related to the temperature dependence of the kinetic constants and to different supersaturation conditions.

In order to fit the model kinetic parameters, a correct and stable procedure has to be developed. Unfortunately, this is usually a hard task as, in this so-called inverse problem, the correspondence between experimental absorbance and size distribution is not unique: different PSD could have the same second moment and consequently lead to same absorbance values. To overcome this problem and to obtain sound results, some parameter values were not regressed. For example, the exponents of nucleation and growth expressions were assumed to be $a = 2.1$ and $b = 1.5$, respectively, according to the range of values reported in the literature (see, for example, Zauner and Jones, 2000). A sequential procedure was used for other parameters: nucleation and growth-rate constants were obtained from the maximum of the absorbance profiles, and agglomeration and settling frequencies were fitted to experimental data in the last part of the absorbance profiles. Table 2 shows all the parameters used. Note that the

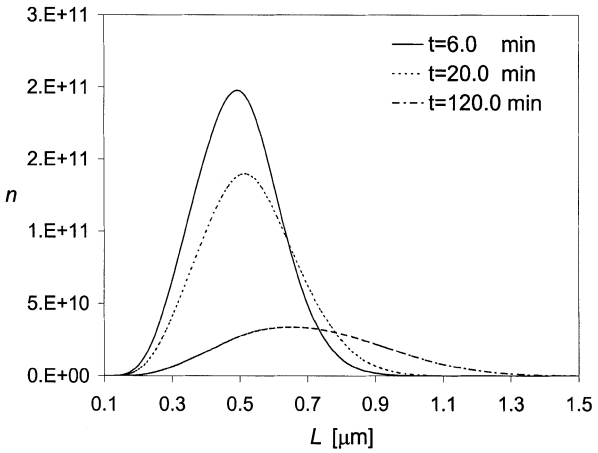

Figure 7. Particle-size distribution as a function of particle size *L* for a case where the growth is dominant.

Numerical solution of Eq.10 at different values of time.

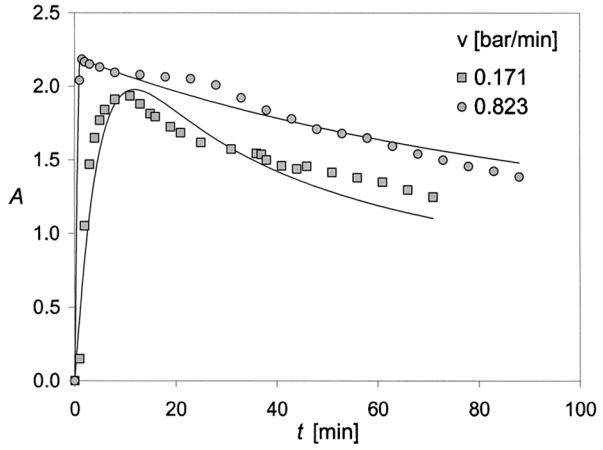

Figure 9. Experimental and calculated absorbance profiles as a function of time for different CO_2 pressurization rates at 307.15 K.

Data points are measured by UV-vis spectrometer for the PLA precipitation from dichloromethane solution. The curves represent the absorbance profile simulated by numerical solution of Eq. 10. The values of model parameters are fitted on the experimental data (see Table 2).

Table 2. Model Parameters that Reproduce Experimental Absorbance Profiles at Different Temperatures and CO_2 Pressurization Rates.*

	$T = 301$ K			$T = 307$ K	
	$\nu = 0.13$ [bar/min]	$\nu = 0.49$ [bar/min]	$\nu = 0.86$ [bar/min]	$\nu = 0.17$ [bar/min]	$\nu = 0.82$ [bar/min]
k_g [μm/s]	5×10^{-6}	5×10^{-6}	9×10^{-4}	5×10^{-6}	9×10^{-4}
k_{aggr} [cm^3/s]	1.2×10^{-16}	2×10^{-15}	9.5×10^{-16}	8×10^{-16}	0.3×10^{-17}
ω	2.2	1.0	0.5	1.0	2.2
$S(t=0)$	4.54	7.31	10.56	5.18	18.00

*The values of these parameters held for all simulation runs: $k_n = 240\times10^6$ [cm$^{-3}\cdot$s^{-1}], $a = 2.1$, $b = 1.5$, k_{sett} 10^{-10} [(μm$^{-2}\cdot$s^{-1}].

values of the nucleation parameters are the same for reproducing all the experiments, whereas the growth rate constant had to be varied (only for the highest pressurization rate). The effect of the pressurization rate was accounted for by estimating the initial supersaturation values on the basis of the equilibrium solubility data of various substances in the solvent/antisolvent systems.

A fair correlation of the experimental profiles was obtained by adjusting the aggregation kernel constant and exponent. On the other hand, it was found that the settling frequency, $k_{sett} = 10^{-10}$ [μm$^{-2}\cdot$s^{-1}] slightly influences the profiles. In summary, parameter values to obtain Figures 8 and 9 differ only as far as aggregation and supersaturation are concerned.

An example of particle-size distribution generated by our model fitted to experimental data points is reported in Figure 10 for two pressurization rates. It is worth noting that a bimodal particle-size distribution is obtained at the highest pressurization rate. Figure 11 shows the simulated PSD of the settled particles. Interestingly, the average particle dimension is very close to that observed in the microparticles collected at the end of the corresponding precipitation experiments.

We are aware that the inverse estimation of the population-balance-model parameters is not always possible by using an averaged property, such as the absorbance of the system. For accurate determination of the precipitation kinetics, additional information would be needed from experimental measurements of the particle-size distribution, which have to be carried out under pressure. For these reasons, the results presented in this work have to be considered as a first contribution toward a rational understanding of the phenomena involved in the gas antisolvent precipitation processes rather than as an exhaustive study of their precipitation kinetics.

Conclusion

The phenomena involved in gas antisolvent precipitation processes were investigated from both an experimental and theoretical point of view. A simple technique based on UV-vis spectroscopy was developed for studying *in situ* the precipitation kinetics of a biodegradable polymer by compressed CO_2. This experimental approach gave an accurate measurement of the absorbance of the system at 600 nm as a function of time.

The influence of single mechanisms on the absorbance of the system was presented through a parametric study based on a population-balance model. It was emphasized that a correct phenomenological representation of the experimental data is possible only if aggregation phenomena are taken into account.

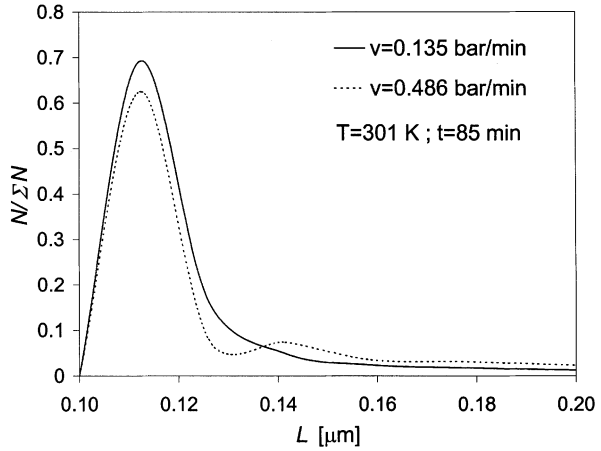

Figure 10. Suspended particle-size distribution as a function of particle size *L*, at 85 min for 0.135 and 0.486 bar/min CO_2 pressurization rates.

The values of model parameters are those used for reproducing the same experimental runs at 301.15 K reported in Table 2.

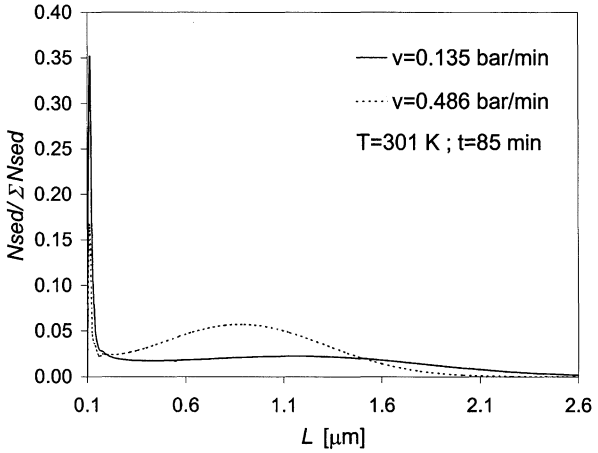

Figure 11. Settled particle-size distribution as a function of particle size, *L*, at 85 min for 0.135 and 0.486 bar/min CO_2 pressurization rates.

The values of model parameters are those used for reproducing the same experimental runs at 301.15 K reported in Table 2.

The particle-size distribution was found to be strongly affected by the aggregation mechanism: a bimodal or unimodal PSD can be obtained at high and low aggregation rates, respectively. A procedure for the estimation of the model parameters was developed. The simulated absorbance profiles give a fair interpretation of the experimental data and, moreover, the particle-size distribution fitted on them well represents the samples collected at the end of the gas anti-solvent precipitation experiments.

Although the parameter estimation procedure could be improved by further experimental measurements, such as the particle size distribution, this study is a first step toward a rational understanding of the precipitation kinetic in gas antisolvent precipitation processes.

Acknowledgments

The authors are grateful to the Italian Ministry for University and Scientific Research (MURST ex 40%) and the University of Padova for partially supporting this work. The precious help of Mr. Lucio Gelmi and Ing. Mara Buzzi in apparatus development is also acknowledged.

Literature Cited

Bleich, J., P. Kleinebudde, and B. W. Mueller, Influence of Gas Density and Pressure on Microparticles Produced with the ASES Process," *Int. J Pharm.*, **106**, 77 (1994).

Dixon, D. J., and K.P. Johnston, "Formation of Microporous Polymer Fibers and Oriented Fibrils by Precipitation with a Compressed Fluid Antisolvent," *J. Appl. Poly. Sci.*, **50**, 1929 (1993).

Draper, S. L., G. A. Montero, B. Smith, and K. Beck, "Solubility Relationships for Disperse Dyes in Supercritical Carbon Dioxide," *Dyes and Pigm.*, **45**, 177 (2000).

Elvassore, N., A. Bertucco and V. Di Noto, "On-line Monitoring Volume Expansion in Gas-Antisolvent processes by UV-vis Spectroscopy," *J. Chem. Eng. Data*, **47**, 223 (2002).

Ernst, M. H., "Kinetics of Clustering in Irreversible Aggregation," *Fractals in Physics*, L. Pietronero, ed., Nort-Holland, Amsterdam (1986).

Gallagher, P. M., M. P. Coffey, V. J. Krukonis, and N. Klasutis, *Supercritical Fluid Science and Technology*, K. P. Johnston and J. M. L. Penninger, eds., ACS Symp. Ser., 334 (1988).

Hounslow, M. J. "A Discretized Population Balance for Continuous Systems at Steady State," *AIChE J.*, **36**, 106 (1990).

Hounslow, M. J., R. L. Ryall, and V. R. Marshall, "A Discretized Population Balance for Nucleation, Growth, and Aggregation," *AIChE J.*, **34**, 1821 (1988).

Ingle, J. D., and S. R. Crouch, *Spectrochemical Analysis*, Prentice Hall, Englewood Cliffs, NJ (1988).

Kelley, S. P., and R. M. Lemert, "Solvatochromic Characterization of the Liquid Phase in Liquid-supercritical CO_2 Mixtures," *AIChE J.*, **42**, 2047 (1996).

Kim, S., and K. P. Johnston, "Molecular Interaction in Dilute Supercritical Fluid Solution," *Ind. Eng. Chem. Res.*, **26**, 1206 (1987).

Litster, J. D., D. J. Smit, and M. J. Hounslow, "Adjustable Discretized Population Balance for Growth and Aggregation," *AIChE J.*, **41**, 591 (1995).

Lora, M., A. Bertucco, and I. Kikic, "Simulation of the Semicontinuous Supercritical Antisolvent Recrystallization Process," *Ind. Eng. Chem. Res.*, **39**, 1487 (2000).

Matson, D. W., J. L. Fulton, R. C. Petersen, and R. D. Smith, "Rapid Expansion of Supercritical Fluid Solution: Solute Formation of Powders, Thin Films and Fibers," *Ind. Eng. Chem. Res.*, **26**, 2298 (1987).

Mazzotti, M., A. Kessler, M. Müller, and U. Meier, "Experimental Study of the Effect of Process Parameters in the Recrystallization of an Organic Compound Using Compressed Carbon Dioxide as Antisolvent," *Ind. Eng. Chem. Res.*, **39**, 2260 (2000).

Perry, R. H., and D. W. Green, *Perry's Chemical Engineers' Handbook*, 7th ed., McGraw-Hill, New York (1997).

Randolph, A. D., and M. A. Larson, *Theory of Particulate Processes*, 2nd ed., Academic Press, San Diego (1988).

Rawlings, J. B., S. M. Miller, and W. R. Witkowski, "Model Identification and Control of Solution Crystallization Processes: A Review," *Ind. Eng. Chem. Res.*, **32**, 1275 (1993).

Reverchon, E. "Supercritical Antisolvent Precipitation of Micro- and Nano-Particles," *J. Supercritic. Fluids*, **15**, 1 (1999).

Reverchon, E., and M. Perrut, "Particle Design Using Supercritical Fluids: Review and Examples," *Proc. Meeting on Supercritical Fluids*, Antibes, France (2000).

Subramaniam, B., R. A. Rajewski, and K. Snavely, "Pharmaceutical Processing with Supercritical Carbon Dioxide," *J. Pharm. Sci.*, **86**, 885 (1997).

Toews, K. L., R. M. Shroll, and C. M. Wai, "Ph-Defining Equilibrium Between Water and Supercritical CO_2. Influence on SFE of Organics and Metal Chelates," *Anal. Chem.*, **67**, 4040 (1995).

Werling, J. O., and P. G. Debenedetti, "Numerical Modeling of Mass Transfer in the Supercritical Antisolvent Process," *J. Supercrit. Fluids*, **16**, 167 (1999).

Werling, J. O., and P. G. Debenedetti, "Numerical Modeling of Mass Transfer in the Supercritical Antisolvent Process: Miscible Conditions," *J. Supercrit. Fluids*, **18**, 11 (2000).

Wynn, E. J. W., "Improved Accuracy and Convergence of Discretized Population Balance of Litster et al.," *AIChE J.*, **42**, 2084 (1996).

Zauner, R., and A. G. Jones, "Determination of Nucleation, Growth, Agglomeration and Disruption Kinetics from Experimental Precipitation Data: the Calcium Oxalate System," *Chem. Eng. Sci.*, **55**, 4219 (2000).

Manuscript received Oct. 1, 2001, and revision received Sept. 10, 2002.